Nano Research

ISSN 1998-0124 CN 11-5974/O4
https://doi.org/10.1007/s12274-022-4826-0

Research Article

Quick photofabrication of functional nanospheres from *de novo* designed peptides for NIR fluorescence and MR imaging

Jingyi Zhao[1], Chen Li[1], Xue-Wang Gao[2], Ke Feng[2], Hao Liu[1], Sijie He[1], Wenhua Zhao[1], Shumin Yang[1], Jianqun Shao[1], Ling Ye[1], Bin Chen[2], Nan Xie[1] (✉), Chen-Ho Tung[2], and Li-Zhu Wu[2] (✉)

[1] *School of Pharmaceutical Sciences, Capital Medical University, Beijing 100069, China*
[2] *Key Laboratory of Photochemical Conversion and Optoelectronic Materials, Technical Institute of Physics and Chemistry, Chinese Academy of Sciences, Beijing 100190, China*

Received: 4 May 2022 / **Revised:** 24 July 2022 / **Accepted:** 27 July 2022

ABSTRACT

Combining the noncovalent and covalent interactions, a series of peptide amphiphiles were designed *de novo* and synthesized to architect functional assemblies by means of photochemistry. The strand of peptide sequence was structurally capped with photoactive tyrosine-tyrosine (YY) motifs at both termini, and the spacing was filled by alternating of hydrophilic D (L-aspartate) and hydrophobic X (ε-aminocaproic acid) structure. Upon visible-light irradiation, these *de novo* designed peptides underwent rapid photocrosslinking within merely 10 min. Interestingly, the modulation of alternating D–X pairs in occupying spacer would adjust molecular amphiphilicity, regulate charge distribution, and control particle size and loading capacity of peptide nanospheres (PNS) in aqueous media. With entirely peptide-based matrix, this PNS system could host cationic indicators of fluorescent rhodamine and magnetic Gd^{III} for exemplar near infrared (NIR) fluorescence and magnetic resonance (MR) imaging, which paves a pathway to biomaterial and biomedical applications using *de novo* designed peptides.

KEYWORDS

synthetic peptide, photocrosslinking, *de novo* design, encapsulable nanosphere, imaging nanoprobe, dityrosine

1 Introduction

Peptides, as one of the most important building blocks, participate in molecular self-assembly processes to construct senior/secondary structure and three-dimensional (3D) conformation at protein level [1–9]. Benefitting from the features of routine synthesis, sequence encodability, and biological compatibility [7, 8, 10–13], tremendous efforts have been made to mimic bioactive segments with synthetic peptides for use in imaging [14–20], drug delivery [21–27], and tissue engineering [28–31]. Driven by the noncovalent interactions, such as hydrogen bond, π–π stacking, hydrophobic/hydrophilic interaction, and Coulombic impulsion and attraction were recognized as the basic regulations to peptide assembly [2–7], segments like ribbons [32, 33], rods [34–36], sheets [37, 38], tubes [39, 40], and spheres [41, 42] have been created. On the other hand, covalent anchoring, exemplified as disulfide formation or dityrosine crosslink [43, 44], enables to convert peptides from linear to entangled form, lock-in hierarchical conformation, alter biofunction structure, and involve in a series of protein post-translational modification processes [45].

Recently, photochemical synthesis is becoming a powerful toolkit to covalent construction, where incident light is used as a remote source to trigger photoactive species to produce molecules, polymers, and even functional structures [46–48]. Specific peptide residues can be employed as the photoactive sites [49–54]. For instance, disulfide could be derived from cysteine residues upon ultraviolet (UV) irradiation, discrete thiols on peptide amphiphiles took place radical coupling to form hydrogel networks [49]; dityrosine could be photogenerated from tyrosine residues under visible-light [52], affording synthetic shortcut to dityrosine anchors.

Herein, we intend to construct functional nanostructures directly from synthetic peptides by means of photochemistry. In this design, sequence encoding for the peptide primary structure is incorporated by solid phase peptide synthesis (SPPS) and subsequent exposure to visible-light for photofabrication to afford senior structure. Considering the architecting complexity for hierarchical structures, the noncovalent and covalent interactions would work together to guide the sequence encoding of photoactive peptides, and thereby balancing the impact from hydrophilic/hydrophobic properties, pH environment, ionic strength, and spacer occupation. Typically, double-ended tyrosine-tyrosine (YY) is used as the binodal photocrosslinker, negatively charged L-aspartate (D) as the hydrophilic/ionic regulator, and hydrophobic pentamethylene X (ε-aminocaproic acid) as the flexible spacer. An alternating D–X pair is introduced in the strand of peptide sequences, so as to modulate spacer occupation, adjust molecular amphiphilicity, regulate charge distribution, and control particle size and loading capacity. It was expected that visible-light irradiation could be applied to the fabrication of functional assemblies from *de novo* designed peptides to host cationic indicators, such as fluorescent rhodamine and magnetic Gd^{III}, for exemplar near infrared (NIR) fluorescence and magnetic resonance (MR) imaging applications.

Address correspondence to Nan Xie, nanxie@ccmu.edu.cn; Li-Zhu Wu, lzwu@mail.ipc.ac.cn

2 Experimental

2.1 Materials

N-α-Fmoc-L-amino acids, 2-chlorotrityl chloride (CTC) resin, o-benzotriazole-N,N,N',N'-tetramethyluronium hexafluorophosphate (HBTU), and N-hydroxybenzotriazole (HOBt) were purchased from GL Biochem. Tris(2,2'-bipyridiyl)dichloro ruthenium(II) hexahydrate ($Ru(bpy)_3Cl_2·6H_2O$), ammonium persulfate, N-methylmorpholine, and trifluoroacetic acid (TFA) were purchased from Sigma-Aldrich. Rhodamine 800 (Rh800), gadolinium(III) chloride hexahydrate, genistein (GE), chlorpromazine (Cpz), methyl-β-cyclodextrin (β-CD), and wortmannin (WM) were purchased from TCI. MitoTracker Green, LysoTracker Green, and Hoechst 33342 were purchased from KeyGEN Biotech. High-glucose Dulbecco's modified Eagle medium (DMEM), trypsin, fetal bovine serum (FBS), penicillin, streptomycin, and phosphate-buffered saline (PBS) were purchased from Gibco BRL. N,N'-Dimethylformamide (DMF), ethyl ether, and other organic solvents were used as received without further purification.

2.2 Synthesis of YY peptides

The YY peptides were synthesized on CTC resin via standard N-(9-fluorenyl) methoxycarbonyl (Fmoc) solid-phase protocols in DMF. For the coupling of each amino acid (AA), the feeding proportion of AA/HBTU/HOBt was fixed as 4 eq. vs. CTC resin, and N-methylmorpholine was employed as the catalytic base. The removal of Fmoc was performed with 20% piperidine. After solid-phase synthesis, peptides were cleaved from resin by treatment with 95% TFA, 2.5% H_2O, and 2.5% triisopropylsilane for 4 h. Crude products were precipitated in cold ether and collected by filtration. Prior to lyophilization, the deprotected peptides were purified on a reverse-phase Accucore Vanquish C18 column by a Thermo Scientific Vanquish UHPLC with gradient elution using H_2O/acetonitrile (0.05% TFA) as the mobile phase.

NH_2-Tyr-Tyr-Acp-Tyr-Tyr-COOH (YYXYY, 0DYY): High resolution-electrospray ionization mass spectrometry (HR-ESI MS): *m/z* = Cacld. 784.3558, found 784.3560 (err. +0.25 ppm) for $[M + H]^+$, $C_{42}H_{50}N_5O_{10}^+$; Calcd. 806.3377, found 806.3375 (err. −0.25 ppm) for $[M + Na]^+$, $C_{42}H_{49}N_5NaO_{10}^+$; Calcd. 828.3197, found 828.3194 (err. −0.36 ppm) for $[M - H + 2Na]^+$, $C_{42}H_{48}N_5Na_2O_{10}^+$. ^1H nuclear magnetic resonance (NMR) (600 MHz, DMSO-d_6, ppm) *δ*: 12.71 (br, 1H), 9.25 (m, 4H), 8.69 (br, 1H), 7.98 (m, 5H), 7.01 (br, 8H), 6.65 (br, 8H), 4.42 (m, 3H), 3.91 (m, 1H), 2.81 (m, 10H), 1.98 (m, 2H), 1.32 (m, 6H). Anal. Calcd. for $C_{42}H_{49}N_5O_{10}$: C, 64.35; H, 6.30; N, 8.93. Found: C, 64.59; H, 6.01; N, 8.57.

NH_2-Tyr-Tyr-Acp-Asp-Acp-Tyr-Tyr-COOH (YYXDXYY, 1DYY): HR-ESI MS: *m/z* = Cacld. 1,012.4668, found 1,012.4674 (err. +0.59 ppm) for $[M + H]^+$, $C_{52}H_{66}N_7O_{14}^+$; Calcd. 1,034.4487, found 1,034.4490 (err. +0.29 ppm) for $[M + Na]^+$, $C_{52}H_{65}N_7NaO_{14}^+$; Calcd. 1,056.4307, found 1,056.4315 (err. +0.76 ppm) for $[M - H + 2Na]^+$, $C_{52}H_{64}N_7Na_2O_{14}^+$; Calcd. 1,078.4126, found 1,078.4134 (err. +0.74 ppm) for $[M - 2H + 3Na]^+$, $C_{52}H_{63}N_7Na_3O_{14}^+$. ^1H NMR (600 MHz, DMSO-d_6, ppm) *δ*: 12.45 (br, 2H), 9.22 (m, 4H), 8.69 (br, 1H), 7.97 (m, 7H), 7.00 (br, 8H), 6.65 (br, 8H), 4.42 (m, 4H), 3.91 (m, 1H), 2.96 (m, 14H), 2.08 (m, 2H), 1.97 (m, 2H), 1.31 (m, 12H). Anal. Calcd. for $C_{52}H_{65}N_7O_{14}$: C, 61.71; H, 6.47; N, 9.69. Found: C, 62.08; H, 6.21; N, 9.93.

NH_2-Tyr-Tyr-Acp-Asp-Acp-Asp-Acp-Tyr-Tyr-COOH (YYXDXDXYY, 2DYY): HR-ESI MS: *m/z* = Cacld. 1,238.5621, found 1,238.5615 (err. −0.48 ppm) for $[M - H]^-$, $C_{62}H_{80}N_9O_{18}^-$; Calcd. 1,260.5441, found 1,260.5430 (err. −0.87 ppm) for $[M - 2H + Na]^-$, $C_{72}H_{95}N_{11}NaO_{22}^-$; Calcd. 1,282.5260, found 1,282.5248 (err. −0.94 ppm) for $[M - 3H + 2Na]^-$, $C_{72}H_{94}N_{11}Na_2O_{22}^-$. ^1H NMR (600 MHz, DMSO-d_6, ppm) *δ*: 12.38 (br, 3H), 9.22 (m, 4H), 8.69 (br, 1H), 8.00 (m, 9H), 7.01 (br, 8H), 6.65 (br, 8H), 4.43 (m, 5H), 3.92 (m, 1H), 2.97 (m, 18H), 2.08 (m, 4H), 1.98 (m, 2H), 1.33 (m, 18H). Anal. Calcd. for $C_{62}H_{81}N_9O_{18}$: C, 60.04; H, 6.58; N, 10.16. Found: C, 60.58; H, 6.41; N, 9.97.

NH_2-Tyr-Tyr-Acp-Asp-Acp-Asp-Acp-Asp-Acp-Tyr-Tyr-COOH (YYXDXDXDXYY, 3DYY): HR-ESI MS: *m/z* = Cacld. 1,466.6731, found 1,466.6741 (err. +0.68 ppm) for $[M - H]^-$, $C_{72}H_{96}N_{11}O_{22}^-$; Calcd. 1,488.6551, found 1,488.6558 (err. +0.47 ppm) for $[M - 2H + Na]^-$, $C_{72}H_{95}N_{11}NaO_{22}^-$; Calcd. 1,510.6370, found 1,510.6375 (err. +0.33 ppm) for $[M - 3H + 2Na]^-$, $C_{72}H_{94}N_{11}Na_2O_{22}^-$; Calcd. 1,532.6190, found 1,532.6193 (err. +0.20 ppm) for $[M - 4H + 3Na]^-$, $C_{72}H_{93}N_{11}Na_3O_{22}^-$. ^1H NMR (600 MHz, DMSO-d_6, ppm) *δ*: 12.37 (br, 4H), 9.24 (m, 4H), 8.70 (br, 1H), 8.02 (m, 11H), 7.02 (br, 8H), 6.66 (br, 8H), 4.53 (m, 6H), 3.93 (m, 1H), 2.99 (m, 22H), 2.09 (m, 6H), 1.99 (m, 2H), 1.35 (m, 24H). Anal. Calcd. for $C_{72}H_{97}N_{11}O_{22}$: C, 58.88; H, 6.66; N, 10.49. Found: C, 59.13; H, 6.85; N, 10.12.

NH_2-Tyr-Tyr-Acp-Asp-Acp-Asp-Acp-Asp-Acp-Asp-Acp-Tyr-Tyr-COOH (YYXDXDXDXDXYY, 4DYY): HR-ESI MS: *m/z* = Cacld. 1,696.7998, found 1,696.7992 (err. −0.35 ppm) for $[M + H]^+$, $C_{82}H_{114}N_{13}O_{26}^+$; Calcd. 1,718.7817, found 1,718.7805 (err. −0.70 ppm) for $[M + Na]^+$, $C_{82}H_{113}N_{13}NaO_{26}^+$. ^1H NMR (600 MHz, DMSO-d_6, ppm) *δ*: 12.30 (br, 5H), 9.22 (m, 4H), 8.69 (br, 1H), 8.01 (m, 13H), 7.01 (br, 8H), 6.65 (br, 8H), 4.52 (m, 7H), 3.92 (m, 1H), 2.99 (m, 26H), 2.08 (m, 8H), 1.98 (m, 2H), 1.35 (m, 30H). Anal. Calcd. for $C_{82}H_{113}N_{13}O_{26}$: C, 58.04; H, 6.71; N, 10.73. Found: C, 58.59; H, 6.55; N, 10.36.

NH_2-Tyr-Tyr-Acp-Asp-Acp-Asp-Acp-Asp-Acp-Asp-Acp-Asp-Acp-Tyr-Tyr-COOH (YYXDXDXDXDXDXYY, 5DYY): HR-ESI MS: *m/z* = Cacld. 1,924.9108, found 1,924.9080 (err. −1.45 ppm) for $[M + H]^+$, $C_{92}H_{130}N_{15}O_{30}^+$; Calcd. 1,946.8927, found 1,946.8918 (err. −0.46 ppm) for $[M + Na]^+$, $C_{92}H_{129}N_{15}NaO_{30}^+$. ^1H NMR (600 MHz, DMSO-d_6, ppm) *δ*: 12.26 (br, 6H), 9.22 (m, 4H), 8.69 (br, 1H), 8.01 (m, 15H), 7.01 (br, 8H), 6.65 (br, 8H), 4.52 (m, 8H), 3.92 (m, 1H), 2.99 (m, 30H), 2.08 (m, 10H), 1.98 (m, 2H), 1.35 (m, 36H). Anal. Calcd. for $C_{92}H_{129}N_{15}O_{30}$: C, 57.40; H, 6.75; N, 10.91. Found: C, 57.90; H, 6.92; N, 10.63.

2.3 Photofabrication of peptide nanospheres (PNS)

Transparent glass vials containing YY peptide aqueous solution were charged with $Ru(bpy)_3Cl_2$ (1 mol%) and ammonium persulfate (2 eq.), and adjusted to desired pH condition (5, 7, and 9) with NaOH/HCl. Then the scientific vials were mounted on a homemade parallel photoreactor (4 channels) and irradiated from one side upon visible light 405-nm light-emitting diodes (LEDs) (112 $mW·cm^{-2}$, 50 mA direct current (DC) input) for photocrosslinking. The photoreaction mixture was constantly stirred at 300 rpm and maintained at 25 °C by a flow of external cooling system. After 10 min photofabrication, the produced PNS was separated by centrifugation and washed with deionized (DI) water, finally redispersed in aqueous media and served as stock solution for further use. The photocrosslinking yield was calculated based on the weight proportion of dry product to feeding YY peptides.

2.4 Photofabrication of Rh800-loaded peptide nanospheres (Rh@PNS)

Rh@PNS was prepared similar as that of PNS. 3DYY peptide (0.27 mM and pH of 7) was chosen as the optimized condition. Additionally, Rh800 dye (13.5–54.0 μM) was added into the system as the NIR fluorophore. After photofabrication, Rh@PNS was obtained as cyan gel solution. Loading efficiency and encapsulation efficiency were determined by a difference method using the absorbance at 700-nm wavelength.

2.5 Photofabrication of Gd^{III}-loaded peptide nanospheres (Gd@PNS)

Gd@PNS was prepared similar as that of Rh@PNS. Alternatively, $GdCl_3$ (146 μM) was added into the system as the magnetic resonance imaging (MRI) probe. After photofabrication, Gd@PNS was obtained as transparent gel solution. And the gadolinium content was determined by a Varian 710ES instrument with inductively coupled plasma optical emission spectroscopy (ICP-OES).

2.6 Characterizations

High-resolution mass spectrometry experiments were performed on a Thermo Scientific Q-Exactive spectrometer. ^{1}H NMR spectra were recorded on a Bruker Ascend 600 MHz spectrometer and referenced using the residual proton signal of the solvent. Elemental analyses were conducted on a Carlo Erba 1106 elemental analyzer. Fourier transform infrared (FT-IR) spectra were recorded on a Thermo Scientific Nicolet iS5 system. Transmission electron microscopy (TEM) images was conducted by JEM-2100F microscope at accelerating voltage of 200 kV with an EDS. X-ray photoelectron spectroscopy (XPS) was performed on a Thermo Scientific ESCALAB 250Xi spectrometer with a mono X-ray source Al Kα excitation (1,486.6 eV). UV–visible (UV–vis) absorption spectra were recorded on a Shimadzu UV-2600 spectrophotometer. Fluorescence measurements were run on a Hitachi F-2500 fluorescence spectrophotometer. Dynamic light scattering (DLS) and zeta potential (ζ) were determined by a Malvern Nano-ZS90 Zetasizer. Circular dichroism (CD) spectra were measured on a Jasco J-810 spectrometer using 1-mm quartz cuvette. X-ray diffraction (XRD) patterns were obtained by using a Bruker AXS D8 Advance X-ray diffractometer with Cu-Kα radiation (λ = 1.5178 Å).

2.7 Relaxivity measurements

Relaxivity of Gd@PNS was measured with varied concentration of Gd^{3+} on a 7.0-T Bruker PharmaScan Micro-MRI instrument. The pulse sequence was a T_1 map-RATE sequence with the following parameters: repetition times/echo time (TR/TE) = 200, 400, 800, 1,500, 3,000, and 5,000/11 ms; field of view (FOV) = 5.0 cm^2; matrix = 256 mm × 256 mm; slice thickness = 1 mm; and slice thickness = 1 mm. The longitudinal relaxation rate constant r_1 was calculated using a linear fit of the inverse of T_1 relaxation time as a function of [Gd^{3+}].

2.8 Cell viability assay

Human lung adenocarcinoma A549, human hepatoma HepG2, and human umbilical vein endothelial cells (HUVEC) were used to evaluate the performance of PNS. All cells were cultured in DMEM, which was supplemented with 10% FBS, 100 μg·mL^{-1} streptomycin, and 100 U·mL^{-1} penicillin. The growing environmental requires a 5% CO_2 atmosphere with 95% relative humidity at 37 °C. The cytotoxicity of PNS was evaluated on an Enspire multimode microplate reader (PerkinElmer) at wavelength of 570 nm using 3-(4,5-dimethylthiazol-2-yl)-2,5-diphenyltetrazolium bromide (MTT) assay, and details are presented in the Electronic Supplementary Material (ESM).

2.9 Cellular imaging by confocal microscopy

Cells were seeded at a density of 1 × 10^5/well in a 35-mm glass bottom culture dish and cultured overnight. After incubation with Rh@PNS (1 mg·mL^{-1}) for 4 h, the cells were then co-stained with MitoTracker Green, LysoTracker Green, or Hoechst 33342. Organelle-specific imaging of mitochondria, lysosomes, and nuclei was performed on a Leica TCS-SP8 confocal laser scanning microscopy (CLSM). For quantitative analysis of the endocytic pathway, cells were pretreated for 30 min with various inhibitors of genistein (200 μg·mL^{-1}), chlorpromazine (10 μg·mL^{-1}), methyl-β-cyclodextrin (50 μM), and wortmannin (50 nM) prior to the incubation with Rh@PNS.

2.10 Flow cytometry analysis

Cells were seeded in a 6-well plate at a density of 1 × 10^6/well and cultured overnight. After treatment with Rh@NS and inhibitors, the cells were harvested by trypsinization and fixed for 15 min with 4 wt.% paraformaldehyde. The cells were then resuspended in PBS for flow cytometry analysis on a BD LSRFortessa.

2.11 Hemolysis assay

Red blood cells (RBCs) were isolated from fresh mice blood by centrifugation and resuspended in PBS buffer for further testing. For hemolytic analysis, the obtained RBC suspension (0.5 mL) was incubated with Rh@PNS and Gd@PNS (0.5 mL) at varied concentration of 7.81, 15.6, 31.3, 62.5, 125, 250, 500, and 1,000 μM. Deionized water and PBS were used as positive and negative control, respectively. After 2 h incubation, each sample was centrifuged at 3,000 rpm for 10 min, and 200 μL of supernatant was transferred to a 96-well plate. The absorbance of hemoglobin was recorded at 540 nm on a microplate reader to determinate hemolysis ratio: The percent of hemolysis was calculated as follows: Hemolysis% = [(sample absorbance – negative control)/(positive control – negative control)] × 100%.

2.12 *In vivo* imaging, biodistribution analysis, and blood circulation

Female BALB/c mice (6–7 weeks of age) were purchased from the Animal Center of CCMU. All animal experiments or protocols were reviewed and approved by the Animal Ethics Committee of Capital Medical University. Xenograft tumor model was created by subcutaneous implantation of CT26 cells (1 × 10^7 in 50 μL PBS) in flank region of BALB/c nude mice. As the tumors grew approximately 100 mm^3 in volume, the mice were intravenously injected with 200 μL of PNS probes. After anesthetized with isoflurane, the mice were photographed at indicated time intervals. NIR fluorescence imaging was performed on a PerkinElmer IVIS Spectrum imaging system, and MRI was recorded on a 7.0-T Bruker PharmaScan Micro-MRI instrument with multi-slice-multi-echo (MSME) sequences. For biodistribution analysis of Rh@PNS, the mice were sacrificed at 48 h postinjection, and the representative organs including heart, liver, spleen, lung, kidney, and tumor tissue were excised for *ex vivo* NIR fluorescence imaging. For blood circulation of Gd@PNS, the plasma concentrations of Gd^{3+} were monitored on ICP-OES by sampling at 0, 0.5, 1, 2, 4, 8, 12, 24, 48, and 72 h postinjection.

2.13 *In vivo* biosafety analysis

For biosafety evaluation of Rh@PNS and Gd@PNS, BALB/c mice were intravenously injected with 200 μL of PNS probes. At 14 days postinjection, blood samples were collected from orbital sinus by quick removal of the mouse eyeballs for hematological analysis. Major organs were harvested and fixed with 4 wt.% paraformaldehyde, then embedded, sectioned, stained with hematoxylin and eosin (H&E), and examined on a Leica DM6000B microscope.

3 Results and discussion

3.1 Photofabrication of peptide nanoassemblies

For *de novo* design of linear peptide building blocks, the sequence

encoding is guided by a combinatorial concept of noncovalent and covalent interactions. Structurally, the strand of peptide sequence was capped with photoactive YY motifs at both termini, and the spacing was filled by alternating D–X pairs. The design took into account the following reasons: (1) The bilateral dityrosine motifs respond to visible light irradiation to provide covalent-anchored photocrosslinking sites; (2) the alternating pairs of hydrophobic X and hydrophilic D adjust molecular amphiphilicity to facilitate the photofabrication of assemblies; (3) hydrophobic X, bearing flexible pentamethylene structure, modulates the spacer occupation of crosslinkable dityrosine network; and (4) the repeating of negatively charged D regulates the charge distribution of linear peptides as well as corresponding nanoassemblies, and controls the loading capacity of cationic guest probes.

Synthetically, these *de novo* designed peptides could be routinely prepared on CTC resin in DMF via standard Fmoc SPPS. Herein, a series of double-ended YY peptides (*x*DYY, x = 0–5, Fig. 1(a)) were prepared with repeating D–X pairs, definitely characterized by ^{1}H NMR and HR-ESI MS (Figs. S17–S28 in the ESM). All these peptide amphiphiles underwent rapid crosslinking upon visible light irradiation within merely 10 min. During this process, tyrosine was initially photooxidized to tyrosyl radical that would take place coupling reaction with nearby tyrosine to form covalent bond through proton-mediated electron transport [55]. The photofabrication of peptide nanospheres was highly dependent on either pH condition (5, 7, and 9) or the repeating numbers of D–X pairs (*x*DYY peptides, x = 0–5). Transmission electron microscopy (TEM, Table S1 in the ESM) provided a direct comparison of these peptidic assemblies. For lack of hydrophilic D units, the products of 0DYY and 1DYY exhibited strong aggregation after photocrosslinking. The insufficient occupation of hydrophobic spacer X would increase molecular rigidity and restrict spontaneous formation of cascaded nanospheres. While for the D-rich peptide sequences of 4DYY and 5DYY, the photogeneration of nanostructure was suppressed seriously by their excessive solubility in aqueous media, and the prolonged D–X pairs drove discrete distribution of the dityrosine crosslinkers, thus hindering the intermolecular assembling of peptidic building blocks. The moderate D–X pairs endowed the best matching between molecular rigidity and amphiphilicity. Visible light exposure of 3DYY and 2DYY produced core–shell structured PNS through a cascade photocrosslinking pathway (Fig. 1(b) and Fig. S2 in the ESM). At optimized pH condition of 7, aspartate D residues on peptide sequences would be ionized partially in aqueous media, and a delicate balance between molecular charge and hydrophobicity would minimize aggregation and produce well-defined PNS through noncovalent and covalent interactions. Similar to the seed-mediated model [56, 57], the PNS nanoassembly would generate through photocrosslinking upon irradiation and grow gradually till exhausting the feeding peptide in solution. We checked the influence from irradiation time and intensity (Figs. S3 and S4 in the ESM). As shortened the irradiation time to 5 min, the obtained PNS would stick together after treatment because of too soft shell and insufficient crosslinking; while prolonged the irradiation time to 20 min, the PNS product showed no obvious changes, but seemed to be harder than that of 10 min at standard condition (1.35 mM, pH 7, and 112 mW·cm^{-2}@405 nm). The formation of core–shell structure is probably due to a cascaded aging process at different crosslinking level. To make the PNS uniformity, our current strategy is to suppress the photoreaction time and improve dynamics at stabilized condition of feeding peptide concentration, stirring rate, temperature, and radiation distribution.

Further, we monitored the photocrosslinking of 3DYY peptide amphiphile using ^{1}H NMR. As shown in Fig. 1(c), the protons of phenyl group on tyrosine were observed diminished upon 10 min irradiation. Considering the correlation of chemical shifts from tyrosine (H_1 and H_2) to dityrosine (H_a, H_b, and H_c), this photochemical conversion could be calculated as 14.6% based on the decreased integration at 7.02 ppm. On the other side, we monitored the photophysical changes on UV–vis absorption and fluorescence spectroscopies (Figs. 1(d) and 1(e)). A shoulder absorption band arising at 327 nm was accompanied with an

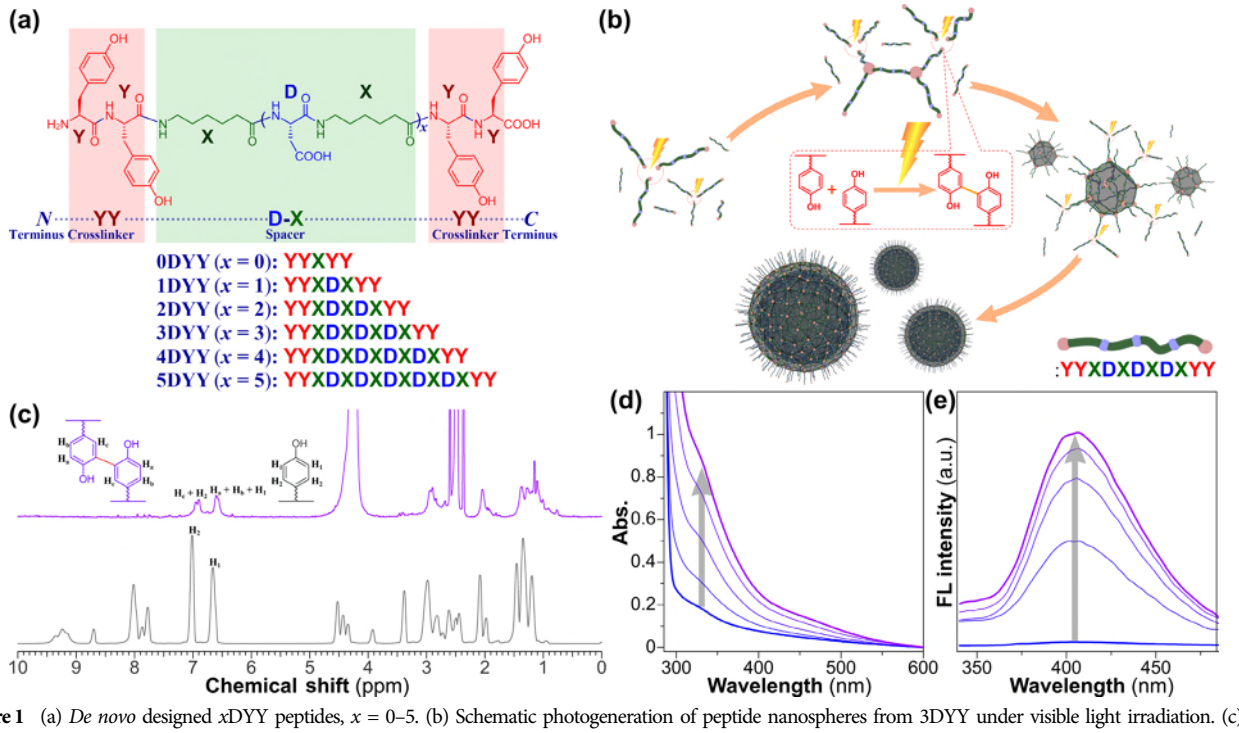

Figure 1 (a) *De novo* designed *x*DYY peptides, x = 0–5. (b) Schematic photogeneration of peptide nanospheres from 3DYY under visible light irradiation. (c) ^{1}H NMR comparison between 3DYY peptide (bottom, in DMSO-d_6) and PNS (top, in DMSO-d_6/D_2O, 9/1). Time-dependent changes of (d) UV–vis absorption and (e) fluorescence emission spectra for 3DYY peptide upon irradiation of 0, 2, 4, 6, and 10 min.

appearance of photoluminescence (PL) at 406 nm, and corresponding intensities were increasing gradually with the prolonged irradiation time. Apparently, it was due to the covalent crosslinking of dityrosine motifs [58].

Through kinetic control of crosslinking, the particle size of PNS could be easily adjusted by the feeding concentration of 3DYY. At low concentration less than 0.1 mM, there were no obvious nanoassemblies observed after photofabrication. At moderate concentration, the particle size of PNS increased with the raising concentration of feeding [3DYY] (Figs. 2(a)–2(c). Fig. 2(c1), 0.27 mM, 109 ± 18 nm; Fig. 2(c2), 1.35 mM, 223 ± 48 nm; and Fig. 2(c3), 2.70 mM, 309 ± 45 nm). As the concentration excessed than 4 mM, irregular aggregates would generate during irradiation. And the variation of PNS particle size was also in accordance with the measurements from DLS (Fig. 2(d). Fig. 2(d1), 154 ± 21 nm; Fig. 2(d2), 243 ± 23 nm; and Fig. 2(d3), 343 ± 46 nm).

Though the morphology of PNS presented highly ordered core–shell structure in high-resolution TEM, the lack of diffraction contrast and lattice fringes indicated its amorphous nature (Fig. 3(b)), which could be confirmed by the absence of characteristic diffuse halo in selected area electron diffraction (SAED, the inset of Fig. 3(b)) pattern and diffraction peak in XRD (Fig. S5 in the ESM). The conformation of 3DYY peptide and its nanoassembly was further compared by CD. After photocrosslinking, PNS well retained the characteristic peaks at 193 and 225 nm, which could be assigned to the β-turn conformation on peptide backbone and the phenolic side chains of tyrosine, respectively (Fig. 3(d)). Additionally, similar FT-IR spectra of 3DYY and PNS (Fig. 3(e)) suggested the continuity in functional groups of hydroxyl O–H (stretch, 3,280 cm^{-1}), aromatic C–H (stretch, 3,078 cm^{-1}), alkyl C–H (methylene, stretch, 2,925 cm^{-1}; methine, stretch, 2,862 cm^{-1}), carbonyl C=O (stretch, 1,716 cm^{-1}), amide (I band, stretch, 1,644 cm^{-1}; II band, stretch, 1,535 cm^{-1}), C–N (stretch, 1,230 cm^{-1}), phenyl–O (stretch, 1,172 cm^{-1}), and aromatic ring on tyrosine (stretch, 1,615, 1,516, and 1,442 cm^{-1}; bending, 830 cm^{-1}).

3.2 Photofabrication of Rh800- and Gd^{3+}-loaded peptide nanoassemblies

For the cationic feature, Rh800 could be easily coassembled into system to obtain Rh@PNS through electrostatic binding with the negatively charged D residues. The reproducibility of nanospherical morphology well retained after photocrosslinking (Fig. 3(f)), and the preferable particle size of Rh@PNS was controlled to 124 nm for less reticuloendothelial system (RES) uptake and prolonged blood circulation. Additionally, the partially

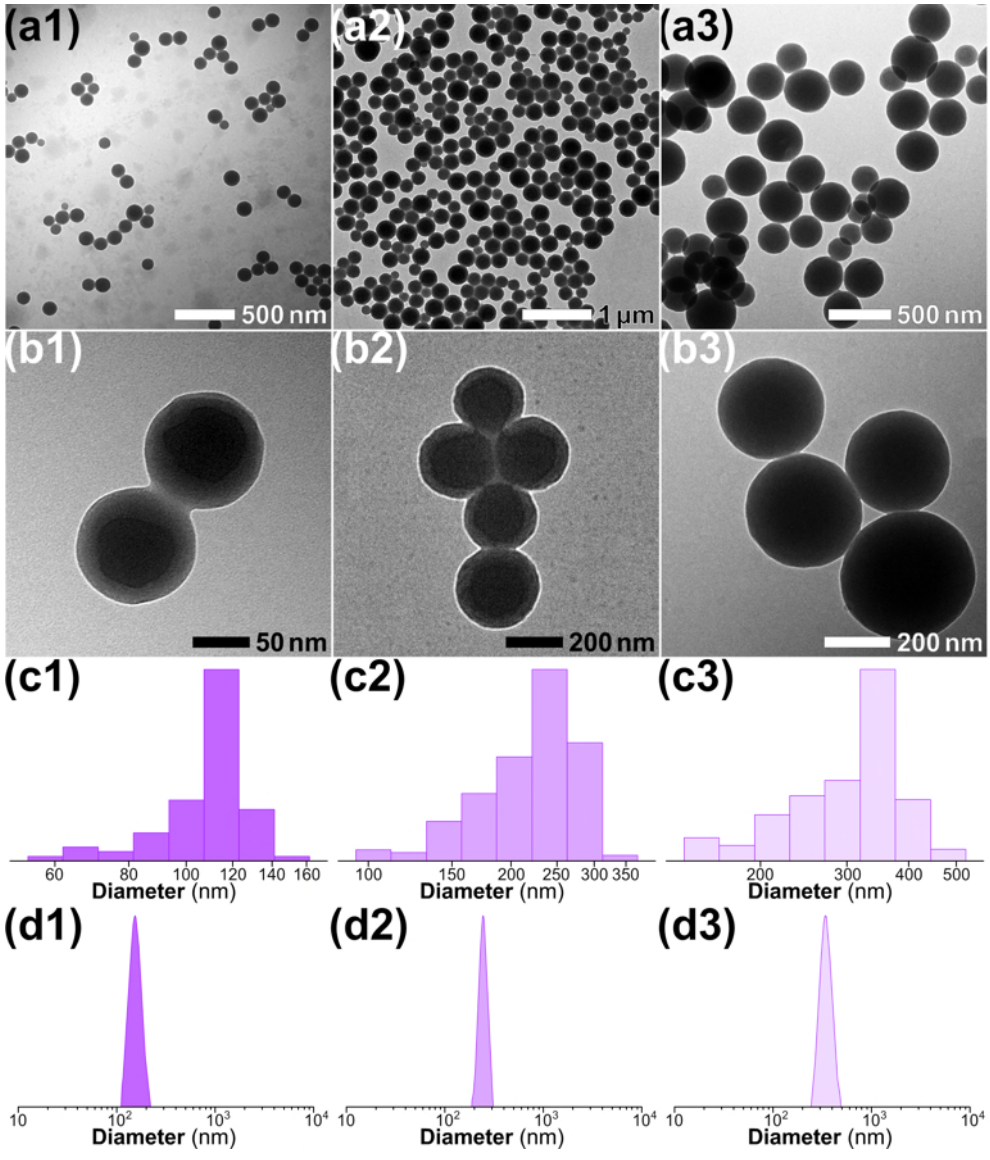

Figure 2 (a) and (b) TEM images, and (c) and (d) corresponding particle size distributions ((c) TEM statistics and (d) DLS measurements) for 3DYY peptide (col. 1, 0.27 mM; col. 2, 1.35 mM; and col. 3, 2.70 mM) after photocrosslinking.

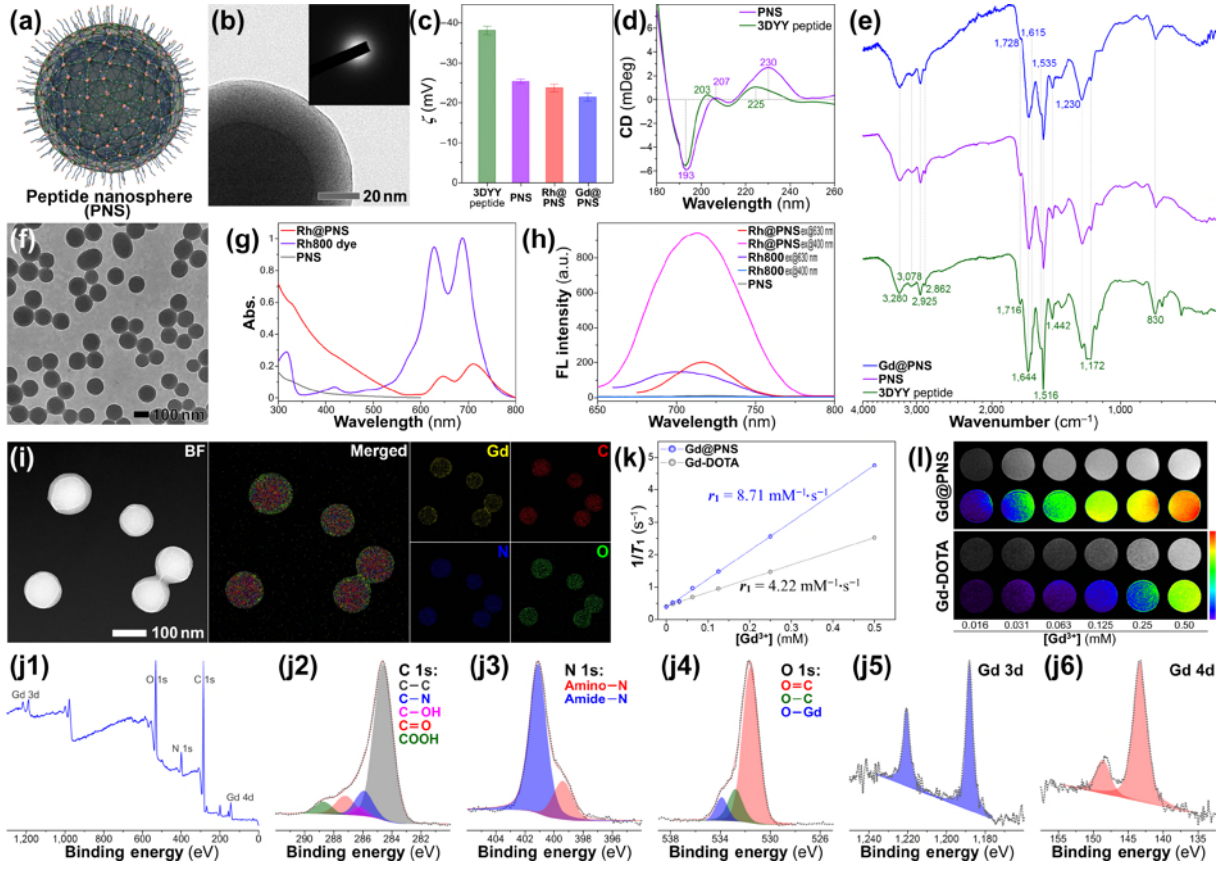

Figure 3 Characterizations of peptide nanospheres. (a) Proposed nanostructure of PNS. (b) High-resolution TEM image and corresponding SAED pattern (inset) of PNS. (c) Zeta potentials of 3DYY peptide, PNS, Rh@PNS, and Gd@PNS. (d) CD spectra of 3DYY peptide and PNS in PBS. (e) FT-IR spectra of 3DYY peptide, PNS, and Gd@PNS. (f) TEM image of Rh@PNS. (g) and (h) UV–vis absorption and fluorescence spectra of PNS, Rh800 dye, and Rh@PNS in PBS. (i) TEM image and corresponding EDS profiles of Gd@PNS. (j) Survey and deconvoluted high-resolution XPS spectra of Gd@PNS. (k) and (l) T_1 relaxivity plots and T_1-weighted images (grayscale, top; pseudo-colored, bottom) of Gd@PNS and Gd-DOTA at varied concentrations.

negative surface in zeta potential of −23.8 mV (Fig. 3(c)) guaranteed its further application to *in vivo* systemic delivery.

The encapsulation of Rh800 in PNS system was monitored by UV–vis absorption spectra, and could be quantitatively evaluated by the characteristic absorbance from Rh800 at 710 nm (Fig. 3(g) and Fig. S6 in the ESM). The loading content varied accordingly with the feeding proportion of Rh800/PNS in the range from 5.2 wt.% to 18.2 wt.% (Table S2 in the ESM). Corresponding encapsulation efficiency of rhodamine dye was as high as 90.0%, even at highest feeding ratio of 20 wt.%, the value still exceeded 78%. It indicated that the coassemble-photocrosslinking strategy could be employed to fabricate functional peptide nanoprobes. Similar to absorbance, slightly bathochromic fluorescence shift was observed in this Rh800-loaded peptide nanospheres (Fig. 3(h)). Compared to free molecules (143 a.u.@700 nm), Rh@PNS presented slight increment (203 a.u.@717 nm) in photoluminescence at same dye concentration. More interestingly, this photoluminescence highly depended on the excitation. As excited at 400 nm, Rh@PNS even exhibited 4.6 times' enhancement in PL intensity at the same measurement configuration. This phenomenon was probably due to light-harvesting effect [59], where biphenyl linkage, dityrosine, could act as the antenna motif and induce Förster energy transfer to Rh800 dye in this encapsulated PNS system.

Paramagnetic Gd^{3+} ion, as a T_1-weighted contrast agent, is often employed to fabricate MRI nanoprobes in hybrid systems. For bearing three units of positive charge, Gd^{3+} exhibited strong electrostatic interaction with 3DYY peptide and could be facilely incorporated in PNS system through photocrosslinking with high encapsulation efficiency (> 90%). The obtained Gd@PNS nanoprobe presented reasonable Gd^{III} loading content according to feeding concentration. TEM photograph confirmed the well retained core–shell structure of PNS after Gd^{III} encapsulation, and the average particle size was observed as 117 nm at optimized condition. Energy dispersive X-ray spectroscopy (EDS, Fig. 3(i)) revealed the coexistence and homogeneous distribution of C, N, O, and Gd elements in this nanoprobes.

XPS further demonstrated the composition and chemical state of Gd@PNS (Fig. 3(j)), and content analysis (C, 52.77%; O, 22.54%; N, 8.02%; and Gd, 11.51%, Table S3 in the ESM) was qualitative in agreement with that from elemental analysis (C, 58.69%; H, 6.72%; and N, 10.15%) and ICP-OES (Gd, 11.61%). Especially, an O–Gd peak was observed at 534.1 eV in XPS (Fig. 3(j4)), indicating the O–Gd coordination through phenol or carboxyl groups in PNS, which was also verified by a slight shift of C=O to higher wavenumbers of 1,728 cm^{-1} in FT-IR spectrum (Fig. 3(e)).

As photofabricated by covalent anchoring, both of Rh@PNS and Gd@PNS nanoprobes exhibited high stability in different aqueous media (deionized water, PBS, and DMEM cell culture medium containing 10% FBS) and pH (5–10) environment (Figs. S7 and S8 in the ESM). The crosslinked dityrosine networks would maintain the structural robustness and integrity for peptide nanoprobes, thus rendering them suitable for wide biological applications.

3.3 *In vitro* biocompatibility and cellular uptake

During MTT test (Fig. S9 in the ESM), both of Rh@PNS and Gd@PNS nanoprobes exhibited no significant cytotoxicities (cell viability > 95%) towards A549, HepG2 tumor cells, and HUVEC normal cells within 3 days' incubation. Moreover, the hemolytic

behavior of PNS was assessed by red blood cell hemolysis (Fig. S10 in the ESM). Compared to the positive control of hemoglobin leaking in DI water, neither Rh@PNS nor Gd@PNS caused notably hemolytic activity, even at high concentration of 1,000 μM, corresponding hemolysis rate was only 1.5% and 0.7%, respectively.

The cellular uptake of Rh@PNS nanoprobe was investigated in A549 and HepG2 tumor cells using CLSM (Figs. S11(a)–S11(c) and S12(a)–S12(c) in the ESM) and flow cytometry analysis (Figs. S11(d), S11(e), S12(d), and S12(e) in the ESM). Strong NIR fluorescence in all three samples indicated the independence on different particle size during cell internalization. Further, the internalization behavior was assessed by independent experiments (Figs. 4(e)–4(g), and Figs. S13 and S14 in the ESM) of 4 °C, GE, Cpz, β-CD, and WM. Quantitative analysis revealed the cellular uptake reduced by more than 90% at low temperature, implying that the peptidic nanoprobe traverses the cell membrane via an energy-dependent pathway. While in the presence of various inhibitors, only GE presented an inhibitory rate of ~ 50%, that acts on tyrosine kinase and blocks caveolae-mediated pathway. We further performed the subcellular localization with commercial LysoTracker or MitoTracker in tumor cells. Rh@PNS nanoprobe presented excellent targeting to lysosomes and exhibited a perfect overlap with LysoTrackers Green (Pearson's *r*, 0.73 ± 0.09, A549; 0.69 ± 0.17, HepG2; Figs. 4(a)–4(d)).

3.4 *In vivo* NIR and MR imaging

Guided by the efficient cellular uptake of Rh@PNS, real-time NIR fluorescence imaging was performed on a subcutaneous xenograft mouse model within 48 h. As the mice treated by Rh@PNS, the NIR fluorescence in tumor region increased gradually with a time-dependent accumulation of nanoprobe and reached a maximum at 16 h post intravenous injection (Fig. 5(a)). While in Rh800-treated mice group, the NIR fluorescence was almost absent at the tumor site (Fig. 5(b)), implying a rapid clearance of molecular dye from blood circulation. In addition, the tumor-selectivity was also evident by comparison in *ex vivo* tissue fluorescence images in Fig. 5(c). Clearly, this specific imaging feature should be attributed to the enhanced permeability and retention (EPR) effect from peptidic nanoprobes. The signal-to-noise ratio (S/N = (mean signal – mean background)/standard deviation of background) and signal-to-background ratio (S/B = mean signal/mean background) of tumor site for Rh@PNS were evaluated as 14.3 and 5.3, respectively, these values are comparable to other representative peptide assemblies [60, 61].

Prior to MRI application, the T_1-weighted relaxivity rate of Gd^{III} encapsulated nanoprobe was evaluated on a 7.0 T magnetic resonance system. As shown in Fig. 3(k), the longitudinal relaxivity (r_1) of Gd@PNS was calculated as 8.71 $mM^{-1}·s^{-1}$, more than twice that of commercial contrast agent, Gd-DOTA (Dotarem, Gd(III)-N,N',N'',N'''-tetracarboxymethyl-1,4,7,10-

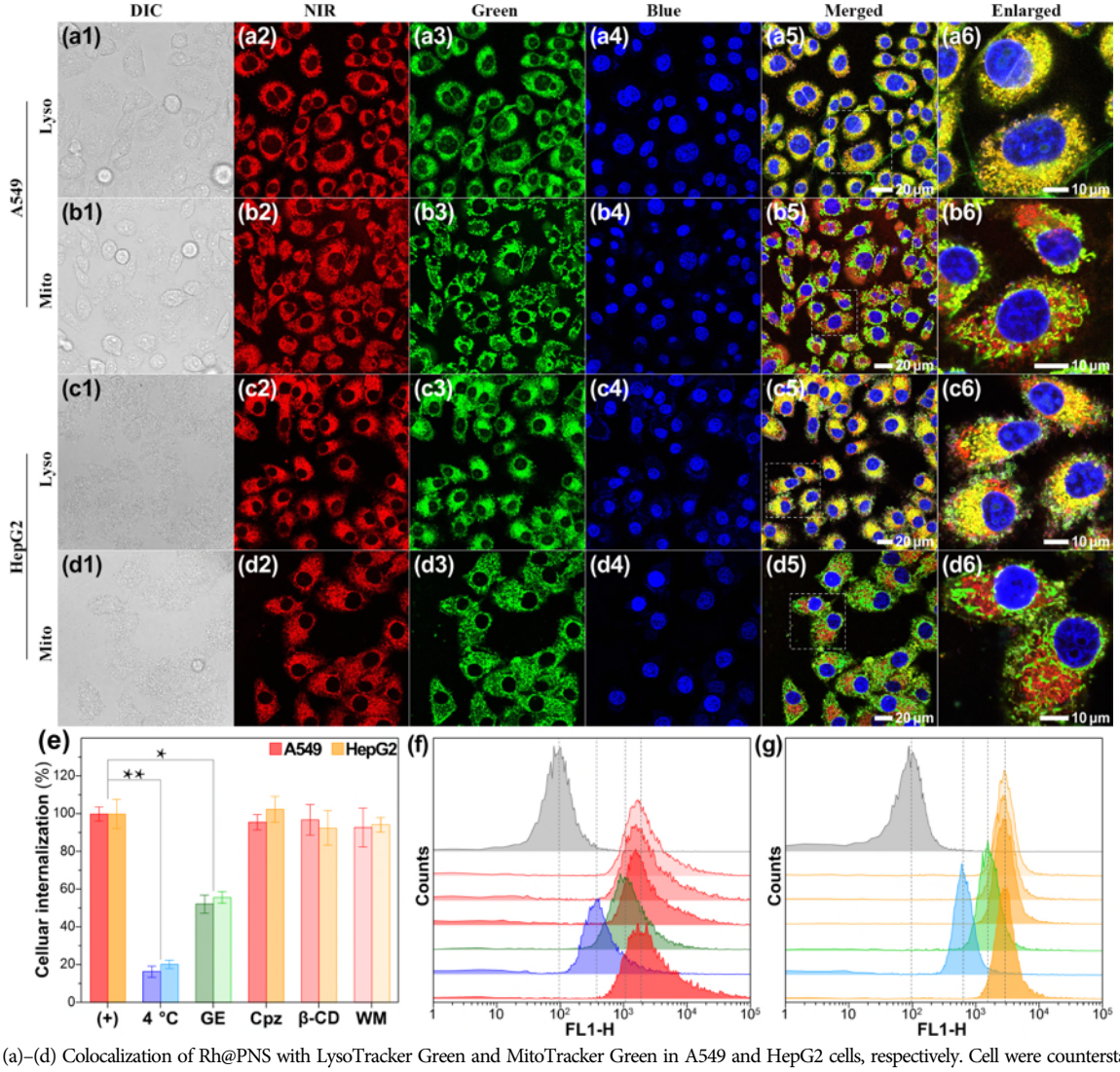

Figure 4 (a)–(d) Colocalization of Rh@PNS with LysoTracker Green and MitoTracker Green in A549 and HepG2 cells, respectively. Cell were counterstained with Hoechst 33342 (blue) for nuclei. Enlarged images are magnified from boxed regions. (e)–(g) Flow cytometry analysis and quantification of Rh@PNS in A549 and HepG2 cells at 4 °C or in the presence of various inhibitors ($n = 3$, $^*p < 0.05$, and $^{**}p < 0.01$).

tetraazacyclododecane, r_1 = 4.22 $mM^{-1}·s^{-1}$). This value is comparable to recent published works (Table S5 in the ESM). Remarkably, the magnetic resonance images of Gd@PNS presented much higher contrast than those of Gd-DOTA at the same Gd^{3+} concentration and apparatus configuration (Fig. 3(l)). This enhancement in proton relaxivity could be ascribed to exceptional stability as well as suitable particle size from the spherical peptide nanostructure, which is beneficial for improving the diagnostic sensitivity at tumor site. Figures 5(d) and 5(e) show the *in vivo* MRI profiles of Gd@PNS in tumor-bearing mice, the T_1-weighted images exhibited maximal brightness and provided discriminative tumor delineation at 16 h post intravenous injection, consistent with the dynamics of Rh@PNS in NIR fluorescence imaging. In comparison, the signals from Gd-DOTA presented weak selectivity in tumor region and quickly faded out to background (Figs. 5(f) and 5(g)). It demonstrated that Gd^{III} encapsulated PNS system could serve as efficient MRI contrast agent and be facilely applied to cancer diagnostics.

The *in vivo* metabolism of Gd^{III} encapsulated PNS could be monitored by blood concentration of Gd^{3+} through ICP-OES. As showed in Fig. 5(i), the kinetic curve of Gd@PNS displayed a relatively long blood circulation lifetime ($t_{1/2}$) of ~ 5 h. In contrast, small-molecular Gd^{III} chelate was rapidly eliminated from the blood compartment, less than half of intravenously injected Gd-DOTA remained after 15 min duration. The tissue accumulation of gadolinium was also examined (Fig. 5(h)). At 24 h post injection, the detected Gd^{3+} content in Gd@PNS treated mice group was more than 15 times that of Gd-DOTA in tumor tissue. This prompt accumulation of Gd@PNS nanoprobe at tumor site could be attributed to the optimized matching between particle size and surface potential in *de novo* designed peptide system, thereby enhancing passive targeting through EPR and facilitating specific tumor imaging.

3.5 *In vivo* biosafety analysis

For hematological analysis, all of key functional indicators, including alanine aminotransferase (ALT), alkaline phosphatase (ALP), aspartate aminotransferase (AST), creatinine (CRE), blood urea nitrogen (BUN), and uric acid (UA), showed no obvious difference between nanoprobes and control groups. It indicated that both of Rh@PNS and Gd@PNS nanoprobes would not impact the physiological functions of liver and kidney (Figs. S15(a) and S15(b) in the ESM). Besides, all blood routine parameters were within the normal ranges and displayed no evident variation (Table S6 and Fig. S16 in the ESM), demonstrating the nonoccurrence of hematopoietic cell damage or inflammatory response in blood test. For histological examination from H&E staining, no appreciable physiological morphology changes and adverse effects were observed in major organs like heart, liver, spleen, lung, and kidney (Fig. S15(d) in the ESM). Additionally, the monitoring on body weight exhibited no significant difference among nanoprobes and control groups (Fig. S15(c) in the ESM). With possession of high biocompatibility and biosafety, these peptide nanoprobes would be suitably applied to a number of biomedical scenarios.

4 Conclusions

In conclusion, we combined noncovalent and covalent interactions together to overcome the structural vulnerability of peptide assembly and photochemically architect functional nanoprobes from synthetic peptides. Structurally, the *de novo* designed peptide sequence was capped with photoactive YY motifs at both termini, and the spacing was filled by alternating D–X pairs. The bilateral dityrosine structure responded to visible light irradiation to generate covalent-anchored multinodes and fabricated PNS in aqueous media within merely 10 min.

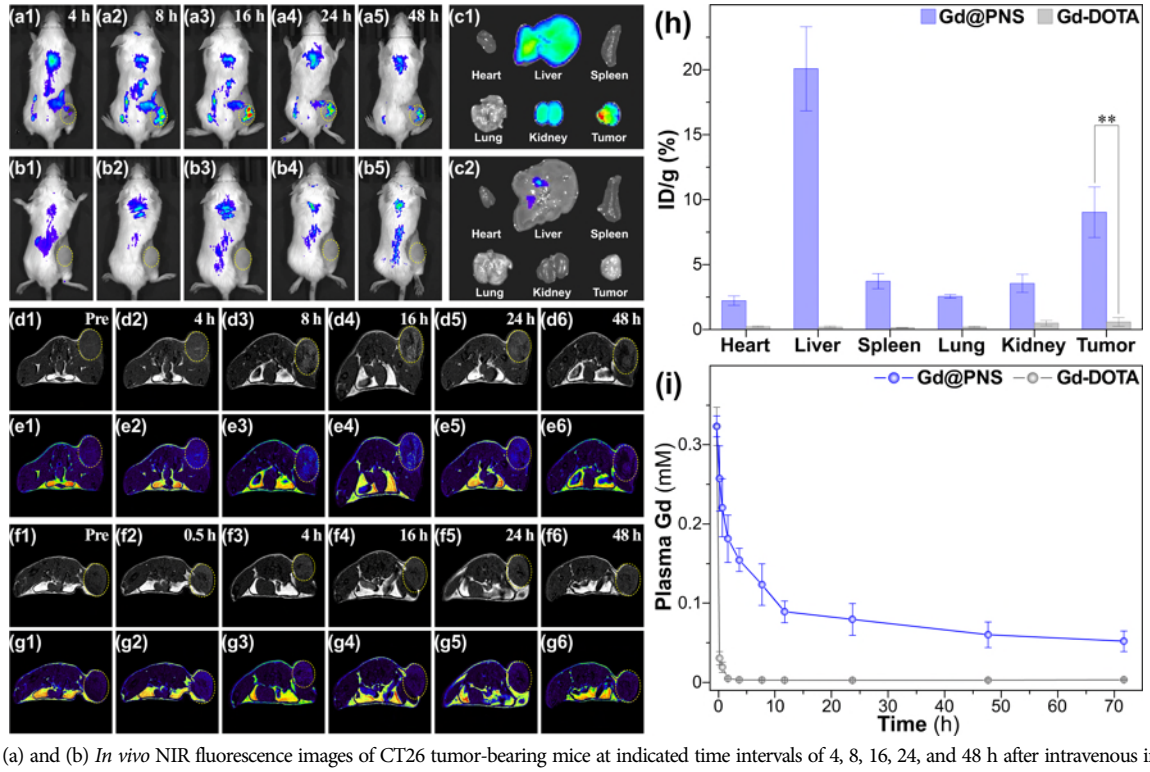

Figure 5 (a) and (b) *In vivo* NIR fluorescence images of CT26 tumor-bearing mice at indicated time intervals of 4, 8, 16, 24, and 48 h after intravenous injection of Rh@PNS and Rh800 at the dose of 0.6 mg·kg^{-1}, based on the feeding amount of Rh800 dye. (c) *Ex vivo* fluorescence images of excised organs and tumors at 48 h post injection of Rh@PNS and free Rh800. (d)–(g) T_1-weighted MRI images of tumors at indicated time intervals of 0, 4 or 0.5, 8, 16, 24, and 48 h after intravenous injection of Gd@PNS and Gd-DOTA at the dose of 0.5 mg·kg^{-1}, based on the feeding amount of Gd^{3+}. The yellow circle showed the tumor site. (h) Quantitative biodistribution of Gd@PNS and Gd-DOTA in various organs at 48 h postinjection (n = 3 and $^{**}p < 0.01$). (i) Plasma concentration of Gd^{3+} at different time postinjection of Gd@PNS and Gd-DOTA (n = 3).

Additionally, the modulation of alternating pairs of hydrophilic D and hydrophobic X in occupying spacer could adjust molecular amphiphilicity, regulate charge distribution, and control particle size and loading capacity. With possession of entirely peptide-based matrix, this PNS system exhibited excellent biocompatibility and biosafety. Utilizing a coassemble-photocrosslinking strategy, the PNS could be further functionalized and host cationic indicators of fluorescent rhodamine and magnetic Gd^{III} for exemplar NIR fluorescence and MR imaging applications. If combined with permutation of peptide sequences in database, this research would pave a more direct pathway from *de novo* designed peptides to biofunctional nanostructures for various biomaterial and biomedical applications.

Acknowledgements

This work was financially supported by Beijing Natural Science Foundation (No. 2222051) and the National Natural Science Foundation of China (No. 81973442). The authors also acknowledge the technical support provided by Core Facility Center at Capital Medical University.

Electronic Supplementary Material: Supplementary material (cell viability assay, additional TEM images and characterization data, stability assessment, hemolysis test, CLSM images and flow analysis for endocytic study, body weights of mice, H&E-stained histological images, blood analysis, and NMR and mass spectra for peptides) is available in the online version of this article at https://doi.org/10.1007/s12274-022-4826-0.

References

[1] Zhang, S. G. Fabrication of novel biomaterials through molecular self-assembly. *Nat. Biotechnol.* **2003**, *21*, 1171–1178.

[2] Aida, T.; Meijer, E. W.; Stupp, S. I. Functional supramolecular polymers. *Science* **2012**, *335*, 813–817.

[3] Abbas, M.; Zou, Q. L.; Li, S. K.; Yan, X. H. Self-assembled peptide- and protein-based nanomaterials for antitumor photodynamic and photothermal therapy. *Adv. Mater.* **2017**, *29*, 1605021.

[4] Feng, Z. Q. Q.; Zhang, T. F.; Wang, H. M.; Xu, B. Supramolecular catalysis and dynamic assemblies for medicine. *Chem. Soc. Rev.* **2017**, *46*, 6470–6479.

[5] Okesola, B. O.; Mata, A. Multicomponent self-assembly as a tool to harness new properties from peptides and proteins in material design. *Chem. Soc. Rev.* **2018**, *47*, 3721–3736.

[6] Wang, J.; Liu, K.; Xing, R. R.; Yan, X. H. Peptide self-assembly: Thermodynamics and kinetics. *Chem. Soc. Rev.* **2016**, *45*, 5589–5604.

[7] Cui, H. G.; Webber, M. J.; Stupp, S. I. Self-assembly of peptide amphiphiles: From molecules to nanostructures to biomaterials. *Pept. Sci.* **2010**, *94*, 1–18.

[8] Hermans, T. M. Materials from a peptide soup. *Nat. Nanotechnol.* **2016**, *11*, 920–921.

[9] Van Tran, V.; Moon, J. Y.; Lee, Y. C. Liposomes for delivery of antioxidants in cosmeceuticals: Challenges and development strategies. *J. Control. Release* **2019**, *300*, 114–140.

[10] Gazit, E. Self-assembled peptide nanostructures: The design of molecular building blocks and their technological utilization. *Chem. Soc. Rev.* **2007**, *36*, 1263–1269.

[11] Hamley, I. W. Peptide nanotubes. *Angew. Chem., Int. Ed.* **2014**, *53*, 6866–6881.

[12] Kumar, M.; Ing, N. L.; Narang, V.; Wijerathne, N. K.; Hochbaum, A. I.; Ulijn, R. V. Amino-acid-encoded biocatalytic self-assembly enables the formation of transient conducting nanostructures. *Nat. Chem.* **2018**, *10*, 696–703.

[13] Lampel, A.; Ulijn, R. V.; Tuttle, T. Guiding principles for peptide nanotechnology through directed discovery. *Chem. Soc. Rev.* **2018**, *47*, 3737–3758.

[14] Qi, G. B.; Gao, Y. J.; Wang, L.; Wang, H. Self-assembled peptide-based nanomaterials for biomedical imaging and therapy. *Adv. Mater.* **2018**, *30*, 1703444.

[15] Zhang, P. C.; Cui, Y. G.; Anderson, C. F.; Zhang, C. L.; Li, Y. P.; Wang, R. F.; Cui, H. G. Peptide-based nanoprobes for molecular imaging and disease diagnostics. *Chem. Soc. Rev.* **2018**, *47*, 3490–3529.

[16] Fan, Z.; Sun, L. M.; Huang, Y. J.; Wang, Y. Z.; Zhang, M. J. Bioinspired fluorescent dipeptide nanoparticles for targeted cancer cell imaging and real-time monitoring of drug release. *Nat. Nanotechnol.* **2016**, *11*, 388–394.

[17] Jiang, Q. C.; Liu, X. Y.; Liang, G. L.; Sun, X. B. Self-assembly of peptide nanofibers for imaging applications. *Nanoscale* **2021**, *13*, 15142–15150.

[18] Hu, B. B.; Song, N.; Cao, Y. W.; Li, M. M.; Liu, X.; Zhou, Z. F.; Shi, L. Q.; Yu, Z. L. Noncanonical amino acids for hypoxia-responsive peptide self-assembly and fluorescence. *J. Am. Chem. Soc.* **2021**, *143*, 13854–13864.

[19] Li, Q.; Zhang, J. X.; Wang, Y. F.; Zhang, G.; Qi, W.; You, S. P.; Su, R. X.; He, Z. M. Self-assembly of peptide hierarchical helical arrays with sequence-encoded circularly polarized luminescence. *Nano Lett.* **2021**, *21*, 6406–6415.

[20] Zhou, Q. Y.; Zhao, T. C.; Liu, M. L.; Yin, D. R.; Liu, M. C.; Elzatahry, A. A.; Zhang, F.; Zhao, D. Y.; Li, Y. M. Highly stable hybrid single-micelle: A universal nanocarrier for hydrophobic bioimaging agents. *Nano Res.* **2022**, *15*, 4582–4589.

[21] Sato, K.; Hendricks, M. P.; Palmer, L. C.; Stupp, S. I. Peptide supramolecular materials for therapeutics. *Chem. Soc. Rev.* **2018**, *47*, 7539–7551.

[22] Abbas, M.; Lipiński, W. P.; Wang, J. H.; Spruijt, E. Peptide-based coacervates as biomimetic protocells. *Chem. Soc. Rev.* **2021**, *50*, 3690–3705.

[23] Tao, K.; Levin, A.; Adler-Abramovich, L.; Gazit, E. Fmoc-modified amino acids and short peptides: Simple bio-inspired building blocks for the fabrication of functional materials. *Chem. Soc. Rev.* **2016**, *45*, 3935–3953.

[24] Sheehan, F.; Sementa, D.; Jain, A.; Kumar, M.; Tayarani-Najjaran, M.; Kroiss, D.; Ulijn, R. V. Peptide-based supramolecular systems chemistry. *Chem. Rev.* **2021**, *121*, 13869–13914.

[25] Shy, A. N.; Kim, B. J.; Xu, B. Enzymatic noncovalent synthesis of supramolecular soft matter for biomedical applications. *Matter* **2019**, *1*, 1127–1147.

[26] Peng, M. Y.; Qin, S. Y.; Jia, H. Z.; Zheng, D. W.; Rong, L.; Zhang, X. Z. Self-delivery of a peptide-based prodrug for tumor-targeting therapy. *Nano Res.* **2016**, *9*, 663–673.

[27] Wang, C.; Piao, J. F.; Li, Y. J.; Tian, X. C.; Dong, Y. C.; Liu, D. S. Construction of liposomes mimicking cell membrane structure through frame-guided assembly. *Angew. Chem., Int. Ed.* **2020**, *59*, 15176–15180.

[28] Gelain, F.; Luo, Z. L.; Zhang, S. G. Self-assembling peptide EAK16 and RADA16 nanofiber scaffold hydrogel. *Chem. Rev.* **2020**, *120*, 13434–13460.

[29] Levin, A.; Hakala, T. A.; Schnaider, L.; Bernardes, G. J. L.; Gazit, E.; Knowles, T. P. J. Biomimetic peptide self-assembly for functional materials. *Nat. Rev. Chem.* **2020**, *4*, 615–634.

[30] Gray, V. P.; Amelung, C. D.; Duti, I. J.; Laudermilch, E. G.; Letteri, R. A.; Lampe, K. J. Biomaterials via peptide assembly: Design, characterization, and application in tissue engineering. *Acta Biomater.* **2022**, *140*, 43–75.

[31] Sinha, N. J.; Langenstein, M. G.; Pochan, D. J.; Kloxin, C. J.; Saven, J. G. Peptide design and self-assembly into targeted nanostructure and functional materials. *Chem. Rev.* **2021**, *121*, 13915–13935.

[32] Pigliacelli, C.; Sanjeeva, K. B.; Nonappa; Pizzi, A.; Gori, A.; Bombelli, F. B.; Metrangolo, P. *In situ* generation of chiroptically-active gold-peptide superstructures promoted by iodination. *ACS Nano* **2019**, *13*, 2158–2166.

[33] Sangji, M. H.; Sai, H.; Chin, S. M.; Lee, S. R.; Sasselli, I. R.; Palmer, L. C.; Stupp, S. I. Supramolecular interactions and morphology of self-assembling peptide amphiphile nanostructures. *Nano Lett.* **2021**, *21*, 6146–6155.

[34] Ji, W.; Tang, Y. M.; Makam, P.; Yao, Y. F.; Jiao, R. R.; Cai, K. Y.;

Wei, G. H.; Gazit, E. Expanding the structural diversity and functional scope of diphenylalanine-based peptide architectures by hierarchical coassembly. *J. Am. Chem. Soc.* **2021**, *143*, 17633–17645.

[35] Zhang, S. S.; Asghar, S.; Zhu, C. Q.; Ye, J. X.; Lin, L.; Xu, L.; Hu, Z. Y.; Chen, Z. P.; Shao, F.; Xiao, Y. Y. Multifunctional nanorods based on self-assembly of biomimetic apolipoprotein E peptide for the treatment of Alzheimer's disease. *J. Control. Release* **2021**, *335*, 637–649.

[36] Xing, P. Y.; Chen, H. Z.; Xiang, H. J.; Zhao, Y. L. Selective coassembly of aromatic amino acids to fabricate hydrogels with light irradiation-induced emission for fluorescent imprint. *Adv. Mater.* **2018**, *30*, 1705633.

[37] Wang, F. B.; Gnewou, O.; Wang, S. Y.; Osinski, T.; Zuo, X. B.; Egelman, E. H.; Conticello, V. P. Deterministic chaos in the self-assembly of β sheet nanotubes from an amphipathic oligopeptide. *Matter* **2021**, *4*, 3217–3231.

[38] Lampel, A.; McPhee, S. A.; Park, H. A.; Scott, G. G.; Humagain, S.; Hekstra, D. R.; Yoo, B.; Frederix, P. W. J. M.; Li, T. D.; Abzalimov, R. R. et al. Polymeric peptide pigments with sequence-encoded properties. *Science* **2017**, *356*, 1064–1068.

[39] Reches, M.; Gazit, E. Casting metal nanowires within discrete self-assembled peptide nanotubes. *Science* **2003**, *300*, 625–627.

[40] Rho, J. Y.; Cox, H.; Mansfield, E. D. H.; Ellacott, S. H.; Peltier, R.; Brendel, J. C.; Hartlieb, M.; Waigh, T. A.; Perrier, S. Dual self-assembly of supramolecular peptide nanotubes to provide stabilisation in water. *Nat. Comm.* **2019**, *10*, 4708.

[41] Brea, R. J.; Devaraj, N. K. Continual reproduction of self-assembling oligotriazole peptide nanomaterials. *Nat. Comm.* **2017**, *8*, 730.

[42] Liu, Y. M.; Shen, G. Z.; Zhao, L. Y.; Zou, Q. L.; Jiao, T. F.; Yan, X. H. Robust photothermal nanodrugs based on covalent assembly of nonpigmented biomolecules for antitumor therapy. *ACS Appl. Mater. Interfaces* **2019**, *11*, 41898–41905.

[43] Schröder, H. V.; Zhang, Y.; Link, A. J. Dynamic covalent self-assembly of mechanically interlocked molecules solely made from peptides. *Nat. Chem.* **2021**, *13*, 850–857.

[44] Zhu, H. T. Z.; Wang, H. H.; Shi, B. B.; Shangguan, L. Q.; Tong, W. J.; Yu, G. C.; Mao, Z. W.; Huang, F. H. Supramolecular peptide constructed by molecular Lego allowing programmable self-assembly for photodynamic therapy. *Nat. Comm.* **2019**, *10*, 2412.

[45] Fass, D.; Thorpe, C. Chemistry and enzymology of disulfide cross-linking in proteins. *Chem. Rev.* **2018**, *118*, 1169–1198.

[46] Li, B. X.; Kim, D. K.; Bloom, S.; Huang, R. Y. C.; Qiao, J. X.; Ewing, W. R.; Oblinsky, D. G.; Scholes, G. D.; MacMillan, D. W. C. Site-selective tyrosine bioconjugation via photoredox catalysis for native-to-bioorthogonal protein transformation. *Nat. Chem.* **2021**, *13*, 902–908.

[47] Chen, B.; Wu, L. Z.; Tung, C. H. Photocatalytic activation of less reactive bonds and their functionalization via hydrogen-evolution cross-couplings. *Acc. Chem. Res.* **2018**, *51*, 2512–2523.

[48] Peng, H. Q.; Niu, L. Y.; Chen, Y. Z.; Wu, L. Z.; Tung, C. H.; Yang, Q. Z. Biological applications of supramolecular assemblies designed for excitation energy transfer. *Chem. Rev.* **2015**, *115*, 7502–7542.

[49] Zhang, Y. N.; Avery, R. K.; Vallmajo-Martin, Q.; Assmann, A.; Vegh, A.; Memic, A.; Olsen, B. D.; Annabi, N.; Khademhosseini, A. A highly elastic and rapidly crosslinkable elastin-like polypeptide-based hydrogel for biomedical applications. *Adv. Funct. Mater.* **2015**, *25*, 4814–4826.

[50] Dumas, A.; Lercher, L.; Spicer, C. D.; Davis, B. G. Designing logical codon reassignment-expanding the chemistry in biology. *Chem. Sci.* **2015**, *6*, 50–69.

[51] Huang, G. Y.; Li, F.; Zhao, X.; Ma, Y. F.; Li, Y. H.; Lin, M.; Jin, G. R.; Lu, T. J.; Genin, G. M.; Xu, F. Functional and biomimetic materials for engineering of the three-dimensional cell microenvironment. *Chem. Rev.* **2017**, *117*, 12764–12850.

[52] Mu, X.; Yuen, J. S. K. Jr.; Choi, J.; Zhang, Y. X.; Cebe, P.; Jiang, X. C.; Zhang, Y. S.; Kaplan, D. L. Conformation-driven strategy for resilient and functional protein materials. *Proc. Natl. Acad. Sci. USA* **2022**, *119*, e2115523119.

[53] Min, K. I.; Kim, D. H.; Lee, H. J.; Lin, L.; Kim, D. P. Direct synthesis of a covalently self-assembled peptide nanogel from a tyrosine-rich peptide monomer and its biomineralized hybrids. *Angew. Chem.* **2018**, *130*, 5732–5736.

[54] Huang, Y. F.; Lu, S. C.; Huang, Y. C.; Jan, J. S. Cross-linked, self-fluorescent gold nanoparticle/polypeptide nanocapsules comprising dityrosine for protein encapsulation and label-free imaging. *Small* **2014**, *10*, 1939–1944.

[55] Fancy, D. A.; Kodadek, T. Chemistry for the analysis of protein–protein interactions: Rapid and efficient cross-linking triggered by long wavelength light. *Proc. Natl. Acad. Sci. USA* **1999**, *96*, 6020–6024.

[56] Nikoobakht, B.; El-Sayed, M. A. Preparation and growth mechanism of gold nanorods (NRs) using seed-mediated growth method. *Chem. Mater.* **2003**, *15*, 1957–1962.

[57] Li, C.; Feng, K.; Xie, N.; Zhao, W. H.; Ye, L.; Chen, B.; Tung, C. H.; Wu, L. Z. Mesoporous silica-coated gold nanorods with designable anchor peptides for chemo-photothermal cancer therapy. *ACS Appl. Nano Mater.* **2020**, *3*, 5070–5078.

[58] Elvin, C. M.; Carr, A. G.; Huson, M. G.; Maxwell, J. M.; Pearson, R. D.; Vuocolo, T.; Liyou, N. E.; Wong, D. C. C.; Merritt, D. J.; Dixon, N. E. Synthesis and properties of crosslinked recombinant pro-resilin. *Nature* **2005**, *437*, 999–1002.

[59] Peng, H. Q.; Chen, Y. Z.; Zhao, Y.; Yang, Q. Z.; Wu, L. Z.; Tung, C. H.; Zhang, L. P.; Tong, Q. X. Artificial light-harvesting system based on multifunctional surface-cross-linked micelles. *Angew. Chem., Int. Ed.* **2012**, *51*, 2088–2092.

[60] An, H. W.; Hou, D. Y.; Zheng, R.; Wang, M. D.; Zeng, X. Z.; Xiao, W. Y.; Yan, T. D.; Wang, J. Q.; Zhao, C. H.; Cheng, L. M. et al. A near-infrared peptide probe with tumor-specific excretion-retarded effect for image-guided surgery of renal cell carcinoma. *ACS Nano* **2020**, *14*, 927–936.

[61] Ren, H.; Zeng, X. Z.; Zhao, X. X.; Hou, D. Y.; Yao, H. D.; Yaseen, M.; Zhao, L. N.; Xu, W. H.; Wang, H.; Li, L. L. A bioactivated *in vivo* assembly nanotechnology fabricated NIR probe for small pancreatic tumor intraoperative imaging. *Nat. Commun.* **2022**, *13*, 418.